Selective 2-Propanol Oxidation over Unsupported Co_3O_4 Spinel Nanoparticles: Mechanistic Insights into Aerobic Oxidation of Alcohols

*Sven Anke[†], Georg Bendt[‡], Ilya Sinev[§], Hamidreza Hajiyani[⊥], Hendrik Antoni[†], Ioannis Zegkinoglou[§], Hyosang Jeon[‖], Rossitza Pentcheva[⊥], Beatriz Roldan Cuenya[‖], Stephan Schulz[‡], Martin Muhler[†,]**

[†] Laboratory of Industrial Chemistry, Ruhr-University Bochum, 44780 Bochum, Germany

[‡] Faculty of Chemistry, Inorganic Chemistry, and Center for Nanointegration Duisburg-Essen (CENIDE), University of Duisburg-Essen, 45114 Essen, Germany

[§] Department of Physics, Ruhr-University Bochum, 44780 Bochum, Germany

[⊥] Department of Physics, Theoretical Physics, and Center for Nanointegration Duisburg-Essen (CENIDE), University of Duisburg-Essen, 47057 Duisburg, Germany

[‖] Department of Interface Science, Fritz-Haber Institute of the Max Planck Society, 14195 Berlin, Germany

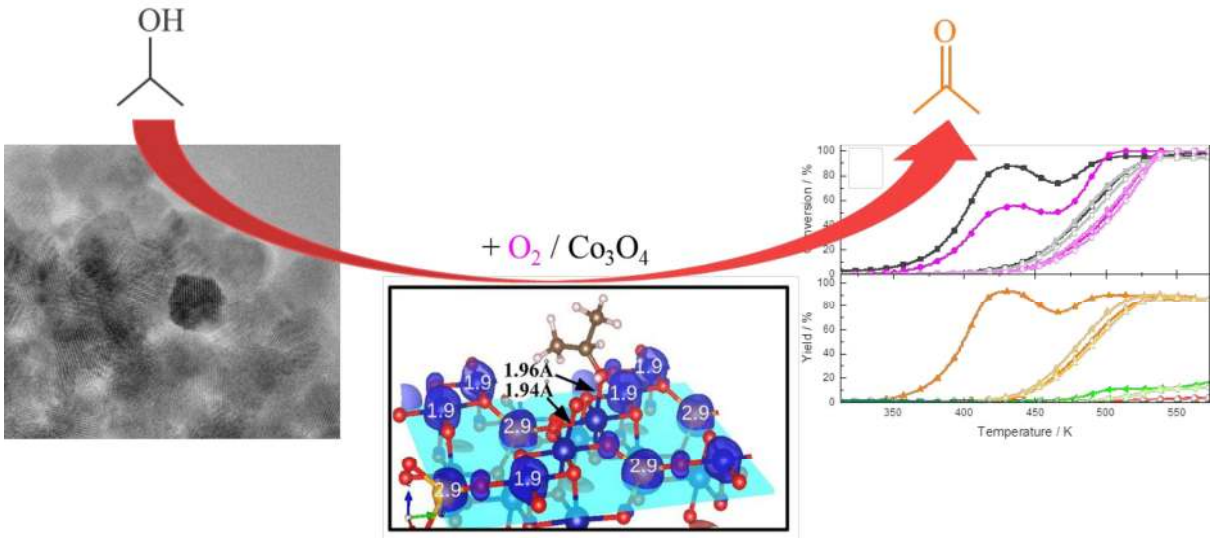

ABSTRACT: Crystalline Co_3O_4 nanoparticles with a uniform size of 9 nm as shown by X-ray diffraction (XRD) and transmission electron microscopy (TEM) were synthesized by thermal decomposition of cobalt acetylacetonate in oleyl amine and applied in the oxidation of 2-propanol after calcination. The catalytic properties were derived under continuous flow conditions as function of temperature up to 573 K in a fixed-bed reactor at atmospheric pressure. Temperature-programmed oxidation, desorption (TPD), surface reaction (TPSR) and 2-propanol decomposition experiments were performed to study the interaction of 2-propanol and O_2 with the exposed spinel surfaces. Co_3O_4 selectively catalyzes the oxidative dehydrogenation of 2-propanol yielding acetone and H_2O and only to a minor extent the total oxidation to CO_2 and H_2O at higher temperatures. The high catalytic activity of Co_3O_4 reaching nearly full conversion with 100% selectivity to acetone at 440 K is attributed to the high amount of active Co^{3+} species at the catalyst surface as well as surface-bound reactive oxygen species observed in the O_2 TPD, 2-propanol TPD, TPSR, and 2-propanol decomposition experiments. Density functional theory calculations with a Hubbard *U* term support the identification of fivefold coordinated octahedral surface Co^{3+}_{5c} as the active site, and oxidative dehydrogenation involving adsorbed atomic oxygen was found to be the energetically most favored pathway. The consumption of surface oxygen and reduction of

Co^{3+} to Co^{2+} during 2-propanol oxidation derived from X-ray absorption spectroscopy and X-ray photoelectron spectroscopy measurements before and after reaction as well as poisoning by strongly bound carbonaceous species result in the loss of the low-temperature activity, while the high-temperature reaction pathway remained unaffected.

KEYWORDS: selective oxidation, Co_3O_4, 2-propanol, surface spectroscopy, DFT+U

1. INTRODUCTION

Catalysts applied in total oxidation reactions often contain noble metals such as gold, platinum or palladium, because catalytic combustion requires very active catalysts as the reaction is performed at high space velocities. They have been intensively investigated for the removal of CO and volatile organic compounds (VOCs) from exhaust emissions.[1–3] In addition, noble metal catalysts are applied in the selective oxidation of alcohols to the corresponding aldehydes and ketones, which is a key technology in chemical industry providing important intermediates for pharmaceuticals and fine chemicals.[4] Many studies focused on selective 2-propanol oxidation over noble metal catalysts supported on different metal oxide materials as probe reaction for the removal of VOC and because of its high suitability to investigate mechanistic aspects.[5–8] It allows identification of intermediates and active sites as well as probing three different reaction routes: dehydrogenation (eq. 1), oxidative dehydrogenation (eq. 2) and dehydration (eq. 3). At high temperatures, the formation of CO_2 is also observed, originating from the total oxidation of 2-propanol (eq. 4) or of reaction intermediates. By performing 2-propanol oxidation, information about the occurring reaction mechanisms and the catalytic properties of the metal or metal oxide can be gained.

$$(CH_3)_2CHOH \rightarrow (CH_3)_2CO + H_2 \quad (1)$$

$$2\ (CH_3)_2CHOH + O_2 \rightarrow 2\ (CH_3)_2CO + 2\ H_2O \quad (2)$$

$$(CH_3)_2CHOH \rightarrow CH_2{=}CHCH_3 + H_2O \quad (3)$$

$$2\ (CH_3)_2CHOH + 9\ O_2 \rightarrow 6\ CO_2 + 8\ H_2O \quad (4)$$

In general, the oxidation reaction proceeds via adsorption of 2-propanol and subsequent formation of 2-propoxide by abstracting the hydroxyl hydrogen. Gong et al.[9] assumed that pre-adsorbed oxygen atoms on Au(111) acts as Brønsted base, which is beneficial for O-H cleavage. They concluded that atomic oxygen is consumed during 2-propanol oxidation, as no O_2 was observed during temperature-programmed desorption (TPD). After dissociative adsorption yielding chemisorbed 2-propoxide, the formation of acetone proceeds by selective β-H elimination and simultaneous desorption of the coupled product water.[5,7] A non-selective C-H bond cleavage is inhibited due to adsorption as 2-propoxide, and subsequently formed acetone desorbs from the catalyst surface. Competing with the formation of acetone, propene can also be formed. C-O bond cleavage was not observed on noble metal catalysts, but over Mo-based catalysts yielding propene.[10] The different reaction mechanisms are ascribed to the differences in the metal-oxygen bond strengths of transition metals.[9] For the adsorption of 2-propanol a Lewis acid-base pair is mandatory. Both reaction pathways require acidic and basic sites, where propene formation takes place at strong acidic and weak basic sites.[6] In contrast, 2-propanol conversion to acetone requires more moderate acidic and strong basic sites.

Noble metal catalysts have several disadvantages and their usage suffers from the tendency to poisoning, high costs, high sintering rates and low thermal stability.[11] In comparison, transition metal oxides possess a higher resistance to poisoning, higher thermal stability and are readily available at low cost.[12] Especially cobalt-based spinel oxides have been studied in several oxidation reactions such as CO oxidation,[13–17] preferential CO oxidation,[18,19] VOC combustion[11,20–22] and selective oxidation of 2-propanol or methanol.[23,24] Gu et al.[25] used the cobalt spinel Co_3O_4 and different Co-containing spinels to investigate the influence of the cobalt oxidation state as well as the coordination number of the cobalt cations in the spinel

structure on the catalytic performance in CO oxidation. Their results indicated that Co^{3+} in octahedral sites is the active site, while Co^{2+} in tetrahedral sites is inactive. Lorenzelli and coworkers[26–29] studied Co_3O_4 as combustion catalyst for various C_3 hydrocarbons and found that cobalt oxide can also be a quite selective oxidation catalyst. They describe the oxidized catalyst as Co_3O_{4+x} with a surface layer, which only contains Co^{3+} coupled with excess oxygen in the form of O^{2-} species and exclude adsorbed molecular oxygen species like O_2, O_2^- or O_2^{2-}. The high reactivity in the oxidation of organic compounds over Co_3O_4 was ascribed to the Co^{3+} centers in the surface layer and the loss in activity to their reduction to Co^{2+}, while the excess oxygen is consumed during oxidation resulting in stochiometric Co_3O_4. For all investigated reactions such as propene, 2-propanol and acetone oxidation, the involved oxygen species was found to be nucleophilic lattice oxygen, even in case of a selective or non-selective oxidation supporting a Mars-van Krevelen-type mechanism. This mechanism was also suggested by Solsona et al.,[30] who studied the oxidation of propane over gold-free and gold-doped Co_3O_4 in a TAP reactor. Nevertheless, Zasada et al.[31] described the activation of O_2 on thermodynamically preferred Co_3O_4 (100) and the presence of various diatomic (superoxo O_2^- and peroxo O_2^{2-}) and monatomic (metal-oxo O^-) reactive oxygen species depending on the adsorption place as well as geometry and the extent of oxygen reduction. Shojaee et al.[32] studied the oxygen stability and vacancy formation on Co_3O_4 (100) and (110) surfaces with different terminations by density functional theory (DFT) calculations suggesting that both surfaces behave differently in oxidation reactions due to differences in binding, oxygen recombination, and oxygen vacancy formation energies. They found on-surface oxygen atoms to be thermodynamically unstable except adsorbed atomic oxygen above bridge sites of cobalt ions which are only located on the (110)-A termination. However, the energy barrier for oxygen recombination keeps oxygen atoms bound at low temperature on other surface terminations. Typically, adsorbed oxygen species are studied by TPD experiments and for Co_3O_4 often three distinct desorption temperatures are reported attributed

to at least three types of oxygen species denoted as α peak, β peak, and γ peak with increasing desorption temperature.[33–35] Unfortunately, various assignments for each peak can be found in literature. Most commonly the α peak is referred to molecular oxygen species, the β peak to atomic oxygen species, and the γ peak to lattice oxygen desorption.

In this study, we report on the catalytic performance of unsupported Co_3O_4 nanoparticles (NPs) in selective 2-propanol oxidation. The catalyst was characterized by X-ray diffraction (XRD), transmission electron microscopy (TEM) and nitrogen physisorption. The interaction with 2-propanol and O_2 was investigated by temperature-programmed methods performed in a fixed-bed reactor and by DFT+*U* calculations. X-ray photoelectron spectroscopy (XPS) before and after 2-propanol oxidation and X-ray absorption spectroscopy (XAS) was used to investigate the influence of the oxidation state of the cobalt species on the catalytic activity.

2. EXPERIMENTAL SECTION

2.1. Catalyst synthesis

For Co_3O_4 NP synthesis 15 mmol $Co(acac)_2$ was suspended in 60 mL of oleylamine. The mixture was heated to 373 K for 10 min to remove low boiling solvents, resulting in a clear red solution. The temperature was then raised to 523 K and kept constant for 60 min. After the solution was cooled to ambient temperature, the resulting Co_3O_4 NPs were precipitated by adding 10 mL of ethanol. The precipitate was isolated by centrifugation, purified by repeated washing (2-3 times) with chloroform/ethanol (1:1) and dried in vacuum. The surfactant oleyl amine was removed from the dried powders by calcination at 573 K for 3 h in air, and the absence of organic residues was shown by IR spectroscopy.

2.2. Catalyst characterization

X-ray diffractograms of the nanoparticles were recorded using a Bruker D8 Advance powder diffractometer with Cu-Kα radiation (λ = 1.5418 Å, 40 kV and 40 mA) and a silicon single crystal as sample holder for minimized scattering. The powder was re-dispersed in

ethanol, deposited on the silicon surface and investigated in the range from 20 to 80° 2θ with a step size of 0.01° 2θ with a counting time of 0.6 s.

Nitrogen physisorption measurements were performed at 77 K in a BELSORP-mini (BEL Japan, Inc.). 200 mg of the sample using a sieve fraction of 250 – 355 µm were pretreated at 473 K for 2 h under vacuum to remove adsorbed water. The specific surface areas were determined from the adsorption isotherm using the BET method. The pore volume and the pore size distribution were obtained by applying the BJH method.

XPS measurements were carried out in an ultra-high vacuum set-up (UHV) equipped with a high resolution Gammadata-Scienta SES 2002 analyzer. A monochromatic Al Kα X-ray source (1486.3 eV; anode operating at 14.5 keV and 30.5 mA) was used as incident radiation and a pass energy of 200 eV was chosen resulting in an energy resolution better than 0.5 eV. Charging effects were compensated using a flood gun. Binding energies were calibrated by positioning the main C 1s peak at 284.5 eV. TEM images of the Co_3O_4 NPs were recorded with a Jeol JEM 2200fs microscope equipped with a probe-side Cs corrector operated at 200 kV acceleration voltage.

X-ray absorption spectroscopy (XAS) was measured at a wiggler beamline CLÆSS[36] of the ALBA synchrotron radiation facility (Barcelona, Spain) operating in a top-up mode. A Si(111) double crystal monochromator was used for the energy scan with de-tuning to 65% of its efficiency to reject higher harmonics. The spectra were recorded in transmission mode at room temperature and during 2-propanol decomposition at fixed temperatures. For the measurements, the Co_3O_4 nanoparticle powder was pressed in a self-supporting pellet and mounted in an *in situ* cell provided by the CLÆSS beamline. A reference metallic foil was measured in each scan to provide an absolute energy calibration. XAS data reduction and fitting was done in the program package "Demeter".[37]

2.3. Experimental procedures

An all stainless-steel microreactor set-up with a calibrated quadrupole mass spectrometer (QMS, Balzers GAM422) was used for the oxidation of 2-propanol. The microreactor consisted of a glass-lined stainless-steel U-tube with an inner diameter of 4 mm, which was heated in an aluminum block oven. For catalytic tests the U-tube reactor was filled with 100 mg of the catalysts (250–355 μm sieve fraction). A thermocouple was directly placed in the catalyst bed for temperature control. Time-resolved quantitative online gas analysis was performed with a QMS, which was calibrated using 0.9608% 2-propanol in He, 9.3191% acetone in He, 1% propene in He, 0.6107% H_2O in He, 0.1% CO_2 in He, and 10% O_2 in He. Dosing of 2-propanol was achieved by passing He through a saturator. The vessels were cooled by means of a cryostat to 273 K, resulting in a saturated mixture of 0.9608% 2-propanol in He. By means of mixing valves 2-propanol/He and O_2 were mixed and further diluted by He. All gas flows were adjusted by calibrated mass flow controllers (MFCs).

Prior to each experiment the catalyst was oxidatively pretreated according to a TPO experiment in 10% O_2/He (10 sccm) for 2 h at various maximum temperatures depending on the following experiment with a heating rate of 3 K min^{-1}, cooled to ambient temperature and purged with He.

For the 2-propanol TPD experiment the catalyst was oxidatively pretreated at 723 K and afterwards 9608 ppm 2-propanol in He (10 sccm) was fed to the reactor until saturation of the sample was reached. The reactor was purged with 10 sccm He for 1 h, until 2-propanol was no longer detected. The saturated sample was heated in He to 723 K with a heating rate of 3 K min^{-1}. For the 2-propanol temperature-programmed surface reaction (TPSR) experiment the procedure was similar, but the saturated sample was heated in 0.18% O_2/He (100 sccm).

For the O_2 TPD experiment the catalyst was initially heated to 723 K in He (10 sccm) and afterwards oxidatively pretreated at maximum temperatures of 373-573 K (50 K steps) and 723 K.

The catalysts used in 2-propanol oxidation and decomposition were oxidatively pretreated at 573 K. For the 2-propanol oxidation experiment the 0.18% 2-propanol/0.18% O_2/He feed gas was passed over the catalyst (100 sccm) for 1 h and the sample was heated to 573 K with a heating rate of 0.5 K min^{-1}. The temperature was kept constant for 1 h before the sample was cooled to ambient temperature with 0.5 K min^{-1}. The 2-propanol oxidation experiment was repeated directly without any further pretreatment. For the decomposition of 2-propanol in the absence of O_2, the procedure was similar, but the initial feed gas was changed to 0.18% 2-propanol/He. For all experiments the reported yields refer to the initial amount of 2-propanol.

2.4. Density Functional Theory calculations

DFT+*U* calculations were performed by using the VASP code with projector-augmented wave (PAW) pseudopotentials.[38–41] The generalized-gradient approximation (GGA-PW91)[42] was used for the exchange-correlation functional, including an on-site Hubbard *U* term. The rotationally invariant approach of Dudarev et al.[43] with $U - J = 3.0$ eV was adopted for the GGA+U calculations. Similar values have been used in our previous studies.[44] The Co_3O_4 (100) surface is simulated using a slab of nine layers with a total of 68 atoms for the bare surface with a vacuum of 15 Å separating the periodic images. To identify the most stable adsorption site, adsorption on top of tetrahedral Co, octahedral Co and O was sampled, including lateral shifts on a dense grid. A plane-wave cut-off of 450 eV and a Monkhorst-Pack k-point mesh of 4×4×1 were used.

3. RESULTS

3.1. Structural characterization

The XRD patterns of the synthesized sample are shown in Figure 1a. The reflections can be assigned to the pure spinel phase Co_3O_4 (PDF2 42-1467). The diffraction patterns with broad reflections indicate the presence of cobalt-based spinel oxide nanoparticles. The TEM images

shown in Figure 1b also confirm that the utilization of the capping agent during synthesis led to almost monodisperse nanoparticles.

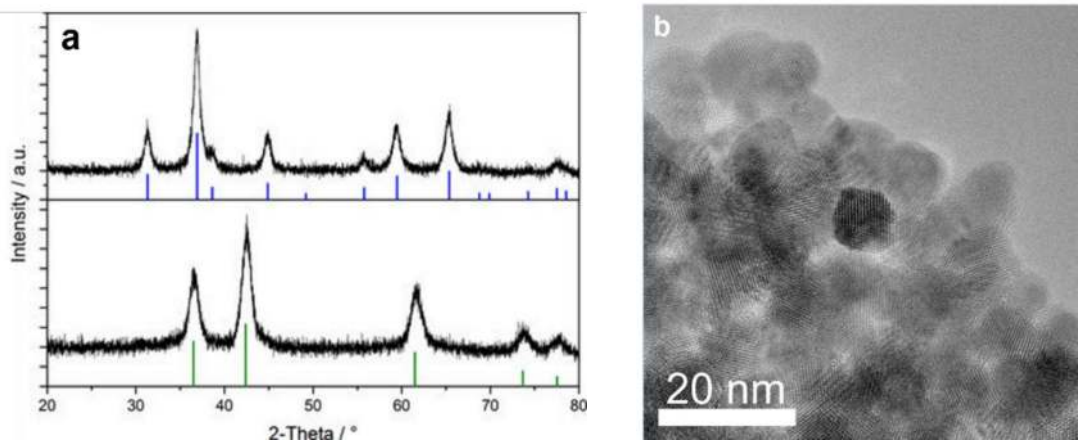

Figure 1. a) XRD patterns of Co_3O_4 before (bottom) and after (top) calcination with references displayed as vertical lines in green (CoO PDF2 02-1079) and blue (Co_3O_4 PDF2 42-1467). b) HR-TEM image of Co_3O_4 NPs.

In addition to the particle size, the results of the N_2 physisorption measurements are summarized in Table 1. The adsorption and desorption curves shown in Figure S1 exhibit type IV isotherms indicating mesoporosity with hysteresis loops similar to H2 and H3 types caused by a complex pore structure. However, porosity arises not from the nanoparticle, but from the voids between them as their size is in good agreement with the nanoparticle size. Assuming non-porous spherical particles the specific surface area can be derived from the particle size according to Rouquerol et al.,[45] but the calculated value is two times larger due to the presence of the interparticle pores. The average interparticle pore diameter of Co_3O_4 is in the mesoporous range and in good agreement with the observed type IV isotherm.

Table 1. Structural properties of the cobalt spinel catalyst.

	particle size[a] / nm	specific surface area / m^2g^{-1}	interparticle pore volume / cm^3g^{-1}	interparticle pore diameter / nm
Co_3O_4	9	43	0.08	7.8

[a] Mean particle size derived from TEM images.

3.2. 2-Propanol TPD

Exposure of Co_3O_4 to 2-propanol at 303 K results in an uptake of 51 µmol/g_{cat} derived from the adsorption curve. All detected effluent mole fractions of the subsequent TPD experiment up to 723 K are shown in Figure 2a. The molecular desorption of 2-propanol as well as the desorption of acetone is detected right after starting the heating ramp, reaching a maximum at 364 K for Co_3O_4. At the same time, the desorption of H_2O is detected with the same desorption maximum at 364 K, indicating an oxidative dehydrogenation process at low temperatures. In addition, a desorption plateau is observed between 581 and 686 K for H_2O. Interestingly, H_2O desorption does not coincide with the desorption of CO_2, since the desorption of CO_2 reaches its maximum at 549 K with two shoulders at 415 K and 500 K, respectively. Neither traces of CO nor of O_2 are detected during the TPD experiment. The desorption profile indicates the formation of acetone at low temperatures via oxidative dehydrogenation (eq. 2) and the formation of CO_2 at higher temperatures via total oxidation due the parallel desorption of the respective products. The observed oxidative dehydrogenation during the TPD experiments clearly indicates the presence of nucleophilic oxygen species, which can be removed from the Co_3O_4 NPs as water resulting in the partial reduction of the exposed oxide surfaces.

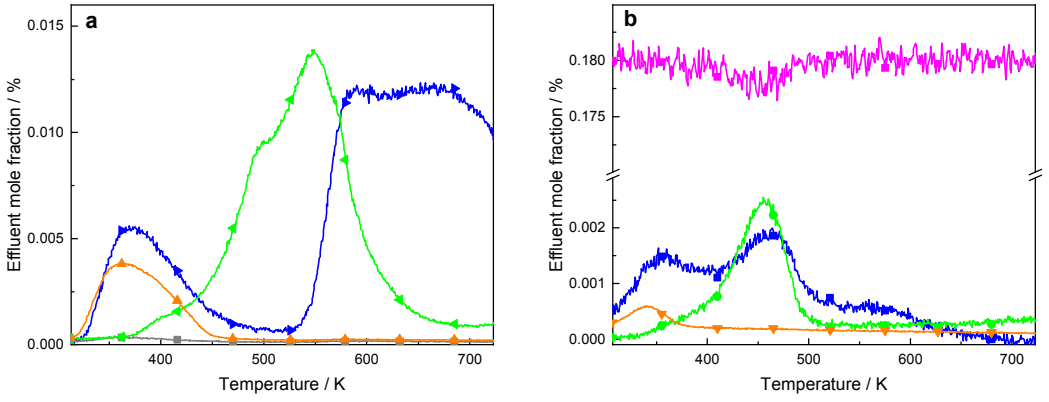

Figure 2. Effluent mole fractions of $(CH_3)_2CHOH$ (■), $(CH_3)_2CO$ (▲), $CH_2{=}CHCH_3$ (▼), CO_2 (◀), H_2O (▶) and O_2 (●) during the 2-propanol TPD (a) and TPSR (b) experiment.

3.3. 2-Propanol TPSR in O_2

Corresponding to the TPD experiments Co_3O_4 was saturated with 2-propanol for the TPSR experiment, but then heated in 0.18% O_2/He. The resulting TPSR profile is shown in Figure 2b. Due to the higher O_2/2-propanol molar ratio the selective product acetone is detected only to a small extent and total oxidation is the dominant reaction. For Co_3O_4 no desorption of 2-propanol is observed. Right after starting the heating ramp the desorption of H_2O and acetone starts with the maxima at 354 K and 343 K, respectively, without any consumption of gaseous O_2. The only O_2 consumption maximum is difficult to observe, but coincides with the desorption maximum of CO_2 and the second desorption maximum of H_2O at 458 K. At temperatures above 500 K only small amounts of desorbed H_2O are detected. The shift of the first H_2O desorption maximum towards higher temperatures compared with the acetone desorption maximum originates from the simultaneously occurring oxidative dehydrogenation and total oxidation reactions. This is indicated by a shoulder, which is observed in the CO_2 profile at slightly higher temperatures than the temperature of the first H_2O maximum. The TPSR experiments reveal that gas-phase oxygen is not participating during oxidative dehydrogenation of pre-adsorbed 2-propanol over Co_3O_4, but it is consumed during total oxidation to CO_2 and H_2O.

The total amounts of detected species during the TPD and TPSR experiments are summarized in Table 2. For both measurements the mass balance cannot be solved, and the ratio of detected carbon and hydrogen atoms do not fit to the initial 3:8 ratio in 2-propanol, indicating that carbon- and hydrogen-containing species remain on the catalyst surfaces. During 2-propanol TPD the total amount of desorbing oxygen atoms is even higher than the amount of adsorbed oxygen atoms present in 2-propanol. Hence, it can be concluded that oxygen surface species are involved in the oxidation of adsorbed 2-propanol.

Table 2. Amounts of detected species during the TPD and TPSR experiments up to 723 K.

Species	n_{des} / µmol g_{cat}^{-1}	
	TPD	TPSR
$(CH_3)_2CHOH$	0.4	0
$(CH_3)_2CO$	4	2
$CH_2=CHCH_3$	0	0
CO_2	24	22
H_2O	42	46
H_2	0	0

3.4 2-Propanol decomposition

The reducibility of Co_3O_4 was probed by a 2-propanol decomposition experiment, which corresponds to a temperature-programmed reduction (TPR) experiment with the reactant as reducing agent. The results are shown in Figure 3. Only low activity was found for Co_3O_4 at low temperatures. To some minor extent 2-propanol was converted starting at 375 K, and traces of acetone, H_2 and H_2O are also observed. Conversion is only slightly increasing up to 460 K, but above this temperature a strong increase is detected. The first maximum is reached at 518 K resulting also in a maximum for acetone (90%) and H_2O (59%). In contrast, the formation of H_2 is still increasing at higher temperatures. The yields of H_2O and H_2 at 518 K sums up to 92% indicating a 1:1 ratio of the oxidative dehydrogenation and dehydrogenation reactions. The small deviation originates from the total oxidation reaction to CO_2, which is only detected in traces. The yield of CO_2 also reaches its first maximum (0.6%) at 518 K, and a further increase in temperature results in the formation of propene reaching a maximum yield of 5% at 552 K. At the maximum temperature more acetone, H_2O, H_2 and small traces of propene and CO_2 (both < 2%) are detected. By comparing the yields of H_2O and H_2 the dominant reaction can be identified: between 470 K and 527 K 2-propanol is mainly converted to acetone via oxidative dehydrogenation (eq. 2), whereas the dehydrogenation reaction (eq. 1) becomes the dominant reaction below and above this temperature range.

Nevertheless, the C:H ratio at high temperatures does not match any reaction stoichiometry as the products are more hydrogen-rich, indicating remaining adsorbed carbonaceous species at the catalyst surface. During cooling 2-propanol conversion and the yields of acetone, propene, CO_2 and H_2O differ significantly. Only minor differences in H_2 yield in the temperature range below 460 K and between 527 K and 573 K are observed. The latter coincides with the temperature range of propene formation during heating, which is not detected during cooling. The 1:1 ratio of the yields of acetone and H_2 during the entire cooling process indicates the selective conversion of 2-propanol by dehydrogenation, whereas the first 2-propanol conversion maximum at 518 K was no longer observed, resulting in a decrease in the yields of acetone, CO_2 and H_2O.

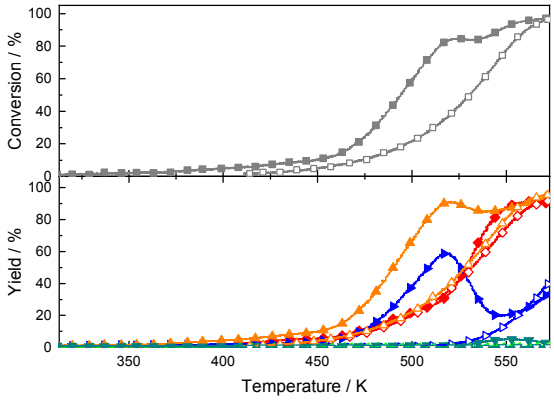

Figure 3. Conversion and yields during 2-propanol decomposition over Co_3O_4 NPs. Conversion of $(CH_3)_2CHOH$ (■) and yields of $(CH_3)_2CO$ (▲), CH_2=$CHCH_3$ (▼), CO_2 (◀), H_2O (▶) and H_2 (♦). Traces with full symbols were obtained during heating and traces with hollow symbols during cooling of the catalyst.

3.5 2-Propanol oxidation

The conversion of 2-propanol and O_2 over Co_3O_4 NPs using a feed gas mixture of 0.18% 2-propanol/0.18% O_2 in He and the corresponding yields are shown in Figure 4 for temperatures between 313 and 573 K. Co_3O_4 is highly active and selective catalyst for 2-propanol oxidation reaching nearly complete 2-propanol conversion at the maximum reaction temperature of 573 K. In comparison to 2-propanol decomposition, the addition of O_2 in the

feed gas leads to an enhanced catalyst activity in the low-temperature region subsequent to the oxidative pretreatment. The onset of conversion is detected at around 330 K giving rise to the first maxima at 430 K for 2-propanol and O_2. At this temperature 2-propanol is converted with 100% selectivity to acetone and H_2O at a ratio of 1:1 indicating oxidative dehydrogenation. The yield of H_2O is not displayed, as H_2O is formed during all relevant reactions, which have different stochiometric ratios regarding 2-propanol and H_2O. Nevertheless, up to the first conversion maximum the yields of acetone and H_2O are equal. Increasing the temperature above 450 K results in a loss of selectivity towards acetone due to total oxidation, and a maximum CO_2 yield of 16% is achieved at the highest reaction temperature. In addition, small traces of H_2 are detected due to complete consumption of O_2, but no evidence of propene formation was found. The yields at the maximum temperature sum up to more than 100% due to the adsorption of 2-propanol at ambient temperature, which is additionally oxidized. Upon cooling to ambient temperature, the conversion of 2-propanol and O_2 and the yield of acetone in the low-temperature region differ significantly from those detected during the first heating cycle. In a subsequent second oxidation experiment without additional oxidative pretreatment the low-temperature maximum is not observed. The degrees of conversion during the second 2-propanol oxidation experiment match the activity observed during cooling in the first oxidation run. The decrease in conversion may result from the consumption of a highly active species or from poisoning of the catalyst influencing the low-temperature maximum at 430 K as well as the first peak of CO_2 at 510 K. In addition, a shift to slightly higher temperatures indicates a small deactivation presumably by carbonaceous species on the catalysts surface for the second run. Additional 2-propanol oxidation runs do not result in a further decrease in activity or change in product selectivity.

After an additional oxidative pretreatment the degrees of conversion shown in Figure 4 coincide with those found during the first oxidation run. The low-temperature maximum in conversion can be restored and is observed at the same temperature yielding the same

amounts of acetone and water. Performing stepwise 2-propanol oxidation with temperature steps at 430 K and 510 K results in a decay of activity during each step. At 430 K 2-propanol conversion decreases strongly within the first hours but reaches a steady state which does not change even after 16 h reaching a higher degree of conversion compared with the performance at the same temperature during the second oxidation run. By increasing the temperature up to 513 K the Co_3O_4 NPs achieve the same catalytic activity as observed during the first oxidation run but keeping the temperature constant again results in a decay of activity. After 16 h no more deactivation is observed, and the degree of 2-propanol conversion coincides with the corresponding conversion during the second oxidation run even after increasing the temperature up to 573 K.

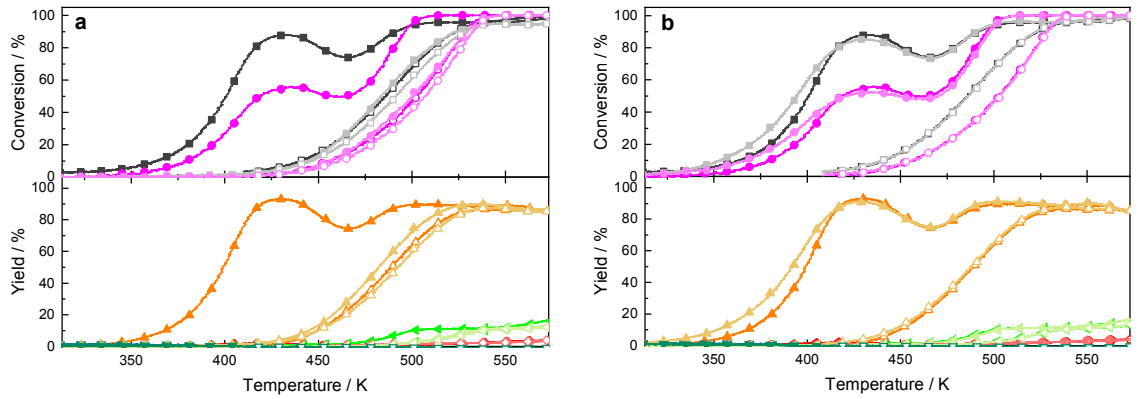

Figure 4. Conversion and yields during (a) the first and subsequent second (lighter colors) and (b) the first and after additional oxidative pretreatment the third (lighter colors) 2-propanol oxidation over Co_3O_4 NPs. Conversion of $(CH_3)_2CHOH$ (■) and O_2 (●) and yields of $(CH_3)_2CO$ (▲), $CH_2{=}CHCH_3$ (▼), CO_2 (◀) and H_2 (♦). Traces with full symbols were obtained during heating and traces with hollow symbols during cooling of the catalyst.

3.6 TPO

The result of the TPO experiment after 2-propanol oxidation is shown in Figure S2. The total amounts of consumed O_2 and formed CO_2 as well as the maximal consumption and desorption temperature (T_{max}), respectively, are summarized in Table 3. For Co_3O_4 one major oxygen consumption is observed, which coincides with the maximum of CO_2 formation and

traces of H_2O. The complete regeneration of the catalyst is already achieved below the maximum temperature desorbing in total 763 µmol g_{cat}^{-1} CO_2. Taking the amounts of consumed O_2 into account, the ratio of detected CO_2 and consumed O_2 is approximately 1:3. The higher amount of consumed O_2 together with the symmetric shape of the oxygen consumption peak and the asymmetric shape of the corresponding CO_2 peak reveal a strong interaction between O_2 and Co_3O_4, which extends beyond the oxidation of residual species adsorbed on the surface.

Table 3. Amounts of consumed O_2 and detected CO_2 and T_{max} during the temperature-programmed oxidation (TPO) up to 573 K.

		Co_3O_4
T_{max}	K	538
consumed O_2	µmol g_{cat}^{-1}	2155
	µmol m^{-2}	50
formed CO_2	µmol g_{cat}^{-1}	763
	µmol m^{-2}	18

3.7 O_2 TPD

To investigate the nature of surface oxygen species on Co_3O_4, O_2 TPD experiments were performed at different pretreatment temperatures (Figure 5). The desorption process sets in around 400 K, but just small amounts of O_2 are detected. Only for the experiment pretreated at the lowest temperature oxygen species already desorb at 360 K. The asymmetric shape of the desorption profiles indicates the superimposition of different O_2 desorption processes. By increasing the pretreatment temperature up to 473 K it was possible to identify at least three low-temperature peaks centered at 400, 438, and 513 K, which are observed as maximum or shoulder in every desorption profile denoted as α_1, α_2, and β_1, respectively. Overall, the desorption maxima are shifted to higher temperatures with increasing pretreatment

temperature. For the desorption experiments at higher pretreatment temperatures, two additional desorption maxima are detected at 613 and 703 K denoted as β_2 and β_3, respectively. The increasing desorption at temperatures above 700 K found for all experiments, except for the pretreatment at 723 K due to superimposition, is denoted as γ peak and can be ascribed to the beginning desorption of surface lattice oxygen. The α peaks are referred to the desorption of surface-bound molecular oxygen species like O_2, O_2^-, or O_2^{2-}, whereas the different β peaks indicate desorption of surface-bound atomic oxygen species from various surface sites.

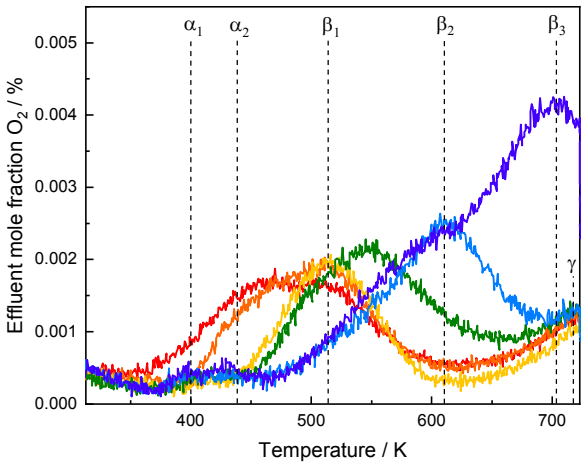

Figure 5. Effluent mole fractions of O_2 during the O_2 TPD experiment over Co_3O_4 NPs oxidatively pretreated at 373 (—), 423 (—), 473 (—), 523 (—), 573 (—), and 723 K (—).

3.8. DFT+*U* Results

Density functional theory (DFT+*U*) calculations were performed to provide insight into the active sites, local geometry and reaction mechanism of 2-propanol oxidation. Both Langmuir-Hinshelwood as well as Mars-van Krevelen pathways involving the participation of lattice oxygen were investigated. Moreover, the role of surface reactive oxygen species (ROS) was also taken into account. The latter have been recently related to the catalytic activity for CO oxidation or N_2O decomposition on cobalt spinel.[16,46,47] We have considered the (100) surface of Co_3O_4 which is abundant under common synthesis conditions.[5] The calculations were performed for the B-layer termination with octahedral cobalt and oxygen, which is stable

under oxygen-rich conditions.[48] Our results indicate that the most favorable sites for adsorption of ROS and 2-propanol are on top of the fivefold coordinated octahedral Co surface sites (Co_{5c}). The spin density of the Co_3O_4 (100) surface without and with adsorbates displayed in Figure 6 gives indication about the oxidation states of surface Co: while the tetrahedral Co is Co^{2+} with a magnetic moment of 2.9 μ_B, surface octahedral Co_{5c} at the bare surface is Co_{5c}^{3+} in the intermediate spin (IS) state with a magnetic moment of 1.9 μ_B. Interestingly, Co underneath both adsorbates 2-propanol and O has the oxidation state of +3 (low spin, LS) as in bulk Co_3O_4. We expect that Co-abundant surfaces (e.g. 0.5 or full A layer terminations or a CoO termination) that are stabilized under oxygen-poor conditions will be enriched in Co^{2+}, as recently found for Fe_3O_4(001).[49]

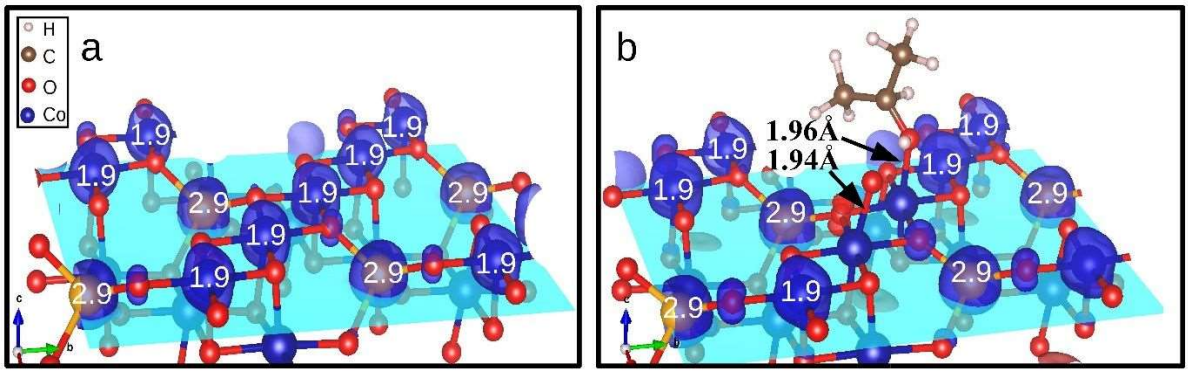

Figure 6. Spin density of (a) the bare Co_3O_4 (100) surface and (b) with adsorbed 2-propanol and ROS at a neighboring site.

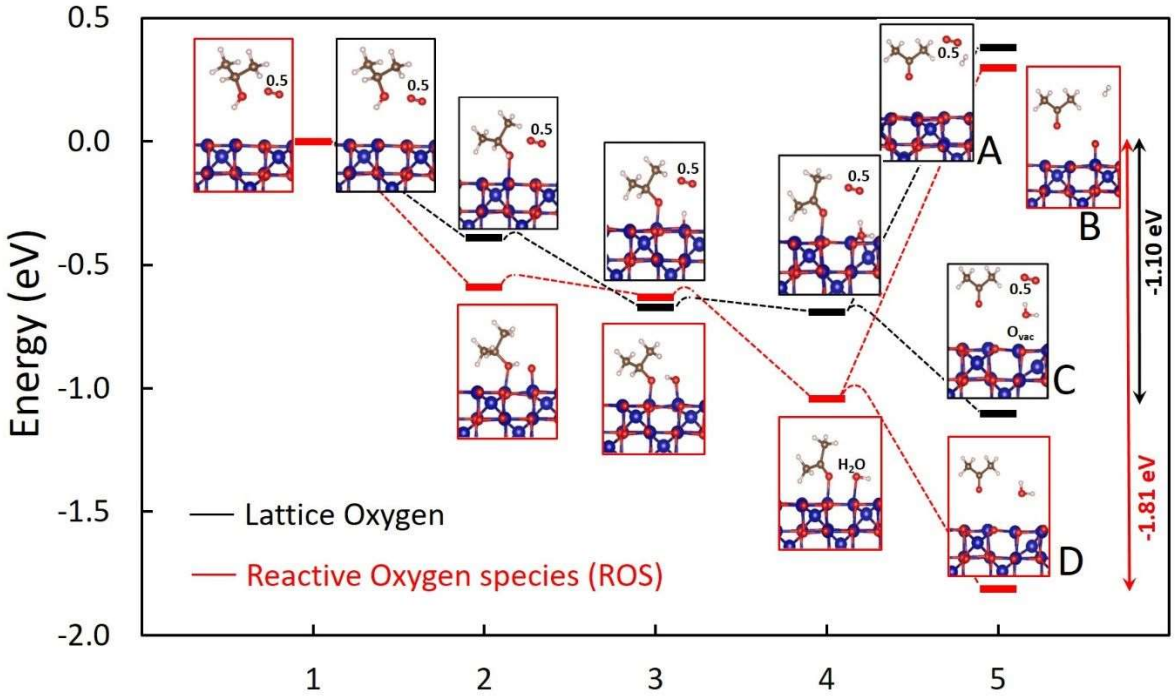

Figure 7. Energetics of intermediates during 2-propanol to acetone oxidation with respect to the initial configuration (2-propanol in the gas phase). Four mechanisms were studied: in A and B acetone desorbs from the surface together with H_2, in C and D the products are acetone and water, in C creating an oxygen vacancy at the surface (Mars-van Krevelen mechanism), in D the oxygen of desorbed water stems from co-adsorbed oxygen on the surface. In the intermediate stages hydrogen from the deprotonation of 2-propanol adsorbs at a surface oxygen or OH group (A,C) or at ROS (D). In order to compare the relative stability of intermediates for the four pathways, $0.5E_{O2}$ is added to the total energy for paths A and C.

In Figure 7 we provide a first assessment of the different mechanisms by comparing the relative stability of intermediates following four paths of 2-propanol to acetone oxidation on the Co_3O_4 (100) surface: the dehydrogenation pathways A and B involve the desorption of acetone and H_2, while the oxidative dehydrogenation pathways C and D result in the formation of acetone and H_2O. They differ, however, concerning the origin of oxygen in the desorbing H_2O molecule: in the Mars-van Krevelen pathway C it stems from a surface/lattice oxygen, leaving a surface with an oxygen vacancy, in the Langmuir-Hinshelwood pathway D

from a co-adsorbed oxygen, leaving a defect-free surface. We note that the co-adsorption of 2-propoxide next to ROS is favored compared with the adsorption on the bare surface. Our results illustrate that the latter pathway D results in the highest energy gain with respect to the initial configuration and compared with the dehydrogenation pathways A and B. As can be seen from Fig. 7, both reaction mechanisms C and D are downhill with higher energy gain for D (-1.81 eV) versus -1.1 eV for C.

3.9. XPS applied before and after reaction

To examine changes in the surface composition during the reaction, the catalysts were analyzed by XPS after oxidative pretreatment and after 2-propanol oxidation. The exposure to air after reaction was minimized by just-in-time transfer to the XPS set-up. The Co oxidation state was examined by Co 2p region scans shown in Figure 8. In the Co 2p spectra the $2p_{3/2}$ and $2p_{1/2}$ peaks as well as the corresponding shake-up satellites are observed. The Co 2p spectra of the catalyst matches typical spectra for pure Co_3O_4 with mixed $Co^{2+/3+}$ oxidation states.[50,51] Usually Co^{2+} exhibits an intense shake-up satellite at 786 eV, whereas for Co^{3+} only a weak satellite peak is formed at 790 eV. Therefore, the Co $2p_{3/2}$ peak at 779 eV and the satellite peak around 787 eV for Co_3O_4 are deconvoluted using five peaks as reported in the literature.[51,50] By comparing the intensity and areas of the fitted curves at 785 eV and 789 eV changes in the oxidation state of the cobalt species are observed. After the O_2 pretreatment the ratio of 1.3 between the areas of the fitted curves at 785 eV and 789 eV is smaller in comparison to the ratio of 2.0 after reaction, indicating a smaller Co^{3+} content after 2-propanol reaction. In addition to the comparison of the shake-up satellites, the energy difference (ΔE) between the $2p_{3/2}$ and $2p_{1/2}$ peaks can be used to examine changes in the Co oxidation state.[52] As suggested by Anantharamaiah and Joy,[53] an energy difference of 15 to 15.4 eV indicates a dominant contribution of Co^{3+}, whereas for Co^{2+}-rich samples ΔE is between 15.7 and 16.1 eV. The energy differences between the $2p_{3/2}$ and $2p_{1/2}$ peaks are

summarized in Table 4. The catalyst shows a higher energy difference after 2-propanol oxidation, indicating a decreased amount of Co^{3+} and an enrichment of Co^{2+} on the surface.

Table 4. Binding energies of the Co $2p_{3/2}$ and $2p_{1/2}$ peaks and corresponding energy differences (ΔE) before and after reaction for Co_3O_4.

	Binding energy / eV		ΔE / eV
	Co $2p_{3/2}$	Co $2p_{1/2}$	
Co_3O_4 before reaction	779.4	794.3	14.9
Co_3O_4 after reaction	779.3	794.5	15.2

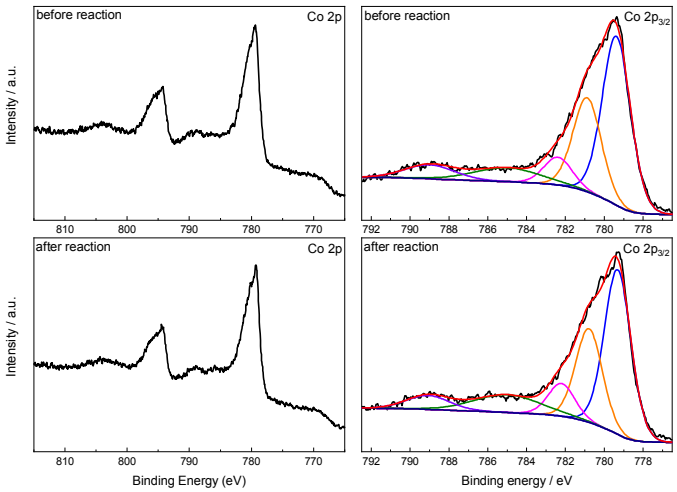

Figure 8. Co 2p spectra and deconvoluted Co $2p_{3/2}$ peaks and satellites of Co_3O_4 NPs before (top) and after (bottom) 2-propanol oxidation.

However, small changes in the oxidation state of cobalt can influence the O 1s spectra after oxidative pretreatment and after reaction as shown in Figure S3. The O 1s peak at 529.5 eV is deconvoluted using three peaks at 529.5 eV, 531.2 eV and 532.8 eV. The peak at 529.5 eV can be assigned to lattice oxygen (O^{2-}), but the assignment of the other peaks at higher binding energies is quite demanding, because they can originate from carbonates (CO_3^{2-}), hydroxides (OH^-), chemisorbed oxygen species (O_2^-, O_2^{2-}, O^-) or adsorbed H_2O. Nevertheless, the O 1s spectra stayed nearly unchanged and only small differences are observed for Co_3O_4 indicating minor changes in the oxide structure.

3.10. XAS

The as-prepared Co_3O_4 NPs resemble the structure of bulk Co_3O_4 as it is seen from X-ray absorption near edge spectra (XANES) in Figure 9a. Thus, the spectrum features a pre-edge peak at 7709.6 eV and a narrow feature above the edge at 7729.9 eV (so-called white line) typical for Co_3O_4 (Figure S4). The corresponding extended X-ray absorption fine-structure spectrum (EXAFS, Figure 10a) shows two main backscattering events at ca. 1.5 and 2.0-3.5 Å (uncorrected for phase shift) corresponding to O as next neighbor and Co as a next-to-next neighbor. The latter structure has a shoulder at 3.0 Å (uncorrected) serving as an extra evidence for the Co_3O_4 spinel structure (see for comparison Figure S5). Spectral EXAFS fitting resulted in Co-O coordination number (CN) close to 4, while the Co-O bond distance (Table S1) is close to that of tetrahedrally coordinated Co^{2+} in Co_3O_4 structure.[54] The CN value is smaller than expected from a mixture of tetrahedral Co^{2+} and octahedral Co^{3+} sites, which can be explained by a dominance of four-fold coordinated divalent cobalt ions in the structure of as-prepared Co_3O_4 NPs.

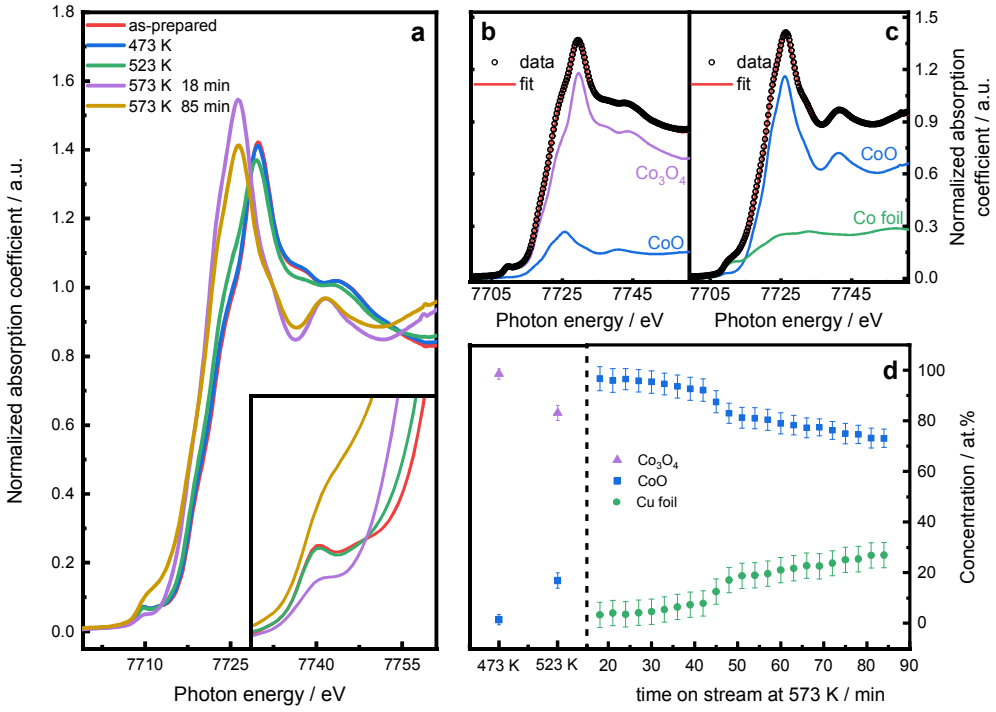

Figure 9. Co K-edge XANES spectra of Co_3O_4 NPs under 2-propanol decomposition conditions measured at different reaction temperatures (a), with the inset showing the zoom-in

of the pre-edge peak region, representative linear combination fits for the spectra measured at 523 (b) and 573 K (c) . Panel d shows composition of the sample depending on the reaction temperature and time on stream at 573 K.

The XAFS measurements of Co_3O_4 during 2-propanol decomposition were carried out at 473, 523, and 573 K in He atmosphere at 1 bar, saturated with 2-propanol vapor by bubbling the gas feed though the liquid at room temperature (5.70% 2-propanol/He). The sample was held for 15 min prior to the first XAS measurements to ensure steady state. First changes in the structure were observed already at 523 K, resulting in a slight shift and decreased intensity of the white line and a shoulder at 7724.3 eV in XANES (Figure 9a). The former suggests the formation of CoO on the surface of the NPs through its interaction with 2-propanol, the relative content of the CoO phase assessed by XANES linear combination analysis (LCA) was found to amount to 17 at% (Figure 9b). Already the first XANES measurement at 573 K resembles the CoO reference (see Figure S4), while the corresponding EXAFS spectrum does not show a shoulder at 3.0 Å assigned to Co_3O_4, indicating a full transformation from the spinel structure of Co_3O_4 to cubic CoO. With further sample exposure to a 2-propanol-containing gas feed, XANES spectra change further – the white line continuously decreases, while the pre-edge feature becomes broader and shifts to higher energy. These changes indicate the further reduction of the Co oxides that became less prominent after ca. 60 min under the feed and the XANES LCA indicates the presence of ca. 27 at% metallic Co (Figure 9c and d). The corresponding EXAFS spectra showed the development of an extra feature at 2.15 Å (uncorrected) representing a Co-Co scattering event, which became first visible after ca. 20 min and continued to grow over time on stream accompanied by a decrease of the EXAFS peaks representing a CoO phase. The highest metallic $Co^{(0)}$-Co CN was found to be 7.9 (Table S1), which corresponds to spherical metallic NPs with ca. 1 nm mean diameter.[55] It has to be noted, however, that the high temperature affects the measurements by decreasing

the EXAFS amplitude and thus the apparent coordination numbers are considerably lower than the real ones corresponding to a given particle size. To offset the temperature effect on the EXAFS spectra, the sample was also measured at room temperature after reaction and cooling in He atmosphere, resulting in a Co-Co CN as high as 9.5, corresponding to a mean NP diameter of ca. 2 nm.

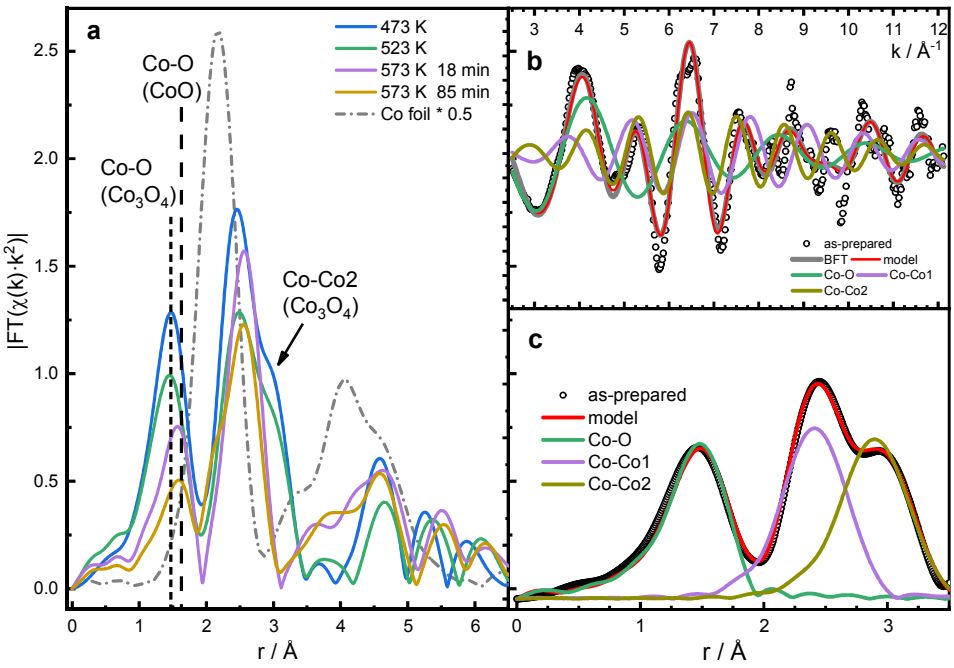

Figure 10. Co K-edge EXAFS spectra of Co_3O_4 NPs under 2-propanol decomposition conditions measured at different reaction temperatures in comparison to a reference spectrum of Co foil, scaled to 0.5 of its intensity for a better display (a). Labels indicate position of the corresponding peaks in bulk Co_3O_4 and CoO references (see Figure S4). Panel b and c illustrate EXAFS fitting if the as-prepared sample in *k*- and *r*-space correspondingly.

4. DISCUSSION

The overall catalytic behavior of unsupported Co_3O_4 in the oxidation of 2-propanol is remarkable with its high activity even at low temperature, mainly catalyzing the oxidative dehydrogenation to acetone and H_2O and to a small extent the total oxidation yielding CO_2 and H_2O only at high temperatures. A high-temperature and a low-temperature reaction pathway are observed. The latter is inhibited after the first heating in the feed gas mixture, but

can be regenerated by oxidative treatment. In TPD and TPSR experiments no or only traces of molecular 2-propanol are detected indicating a high reactivity of Co_3O_4. The high oxidation ability of Co_3O_4 is often ascribed to the $Co^{2+/3+}$ redox properties in close relation to the coordinating oxygen species. This was also observed in this study as the XPS analysis revealed the tendency of partial reduction of Co^{3+} species to Co^{2+} as well as minor changes in the oxygen structure of Co_3O_4 found after 2-propanol oxidation. The reduction behavior of Co_3O_4 under a higher concentration of 2-propanol was followed by XAS measurements. The XANES and EXAFS spectra indicate that the reduction starts higher than 473 K. The formation of CoO on the Co_3O_4 surface was already observed at 523 K and even the formation of metallic Co species was detected at 573 K. The enhanced reducibility compared to the XPS analysis can be explained by the increased 2-propanol content.

Due to the observation of oxidative dehydrogenation in the absence of gas-phase oxygen, the presence of reactive oxygen species on the surface of Co_3O_4 as described by Busca et al.[29] is demonstrated by the TPD, TPSR and 2-propanol decomposition experiments. During the TPSR experiment no consumption of O_2 was detected at low temperature during the formation of acetone and H_2O. In addition, 2-propanol decomposition yielded mainly acetone and H_2O up to 518 K indicating oxidative dehydrogenation in the absence of gas-phase O_2. Therefore, the reaction must involve ROS on the catalyst surface. When surface oxygen is consumed, the H_2O yield drops and an increasing H_2 yield is observed revealing a change from oxidative dehydrogenation to dehydrogenation. During cooling dehydrogenation was also dominant, but in addition to the maximum at 518 K, which was not observed due to consumed oxygen, the conversion maximum at 552 K was also not detected. The reason for the lower activity during cooling of 2-propanol decomposition as well as oxidation may be the reduction of Co^{3+} to Co^{2+} or the blocking of the active sites by carbonaceous species.[27] Residual carbon-containing species are identified by the unsolved mass balance of the TPD and TPSR experiments and by TPO experiment after reaction. In addition, the oxidative

treatment by TPO after reaction regenerates the low-temperature pathway for selective 2-propanol oxidation. The high-temperature pathway also catalyzes oxidative dehydrogenation and at higher temperature total oxidation. Moreover, the pathway is also active in the subsequent second and third 2-propanol oxidation runs with only slightly increased deactivation. The observations point to regeneration due to the removal of carbonaceous residues and a strong interaction of O_2 with Co_3O_4 re-oxidizing the cobalt species and regenerating the ROS. The nature of these species was investigated by O_2 TPD experiments revealing small amounts of surface-bound atomic oxygen species and even small amounts of molecular oxygen species at the Co_3O_4 surface. For the oxidative pretreatment at 573 K, which was also used for 2-propanol oxidation and decomposition, only the β_2 peak and the onset of desorption of surface lattice oxygen species are observed identifying the ROS as surface-bound atomic oxygen species (Scheme 1).

Overall, the results of 2-propanol oxidation over Co_3O_4 fit to the proposed model of the Lorenzelli group,[26–29] in which the organic C3 compound is oxidized at the expense of the surface layer containing exclusively Co^{3+} cations and excess oxygen anions according to the Mars-van Krevelen mechanism. Nevertheless, a contribution of the Langmuir-Hinshelwood mechanism describing the reaction between adsorbed oxygen and adsorbed 2-propanol cannot be excluded due to the strong interaction of oxygen with the Co_3O_4 surface. Indeed, the DFT+*U* results presented here indicate the preference for the latter mechanism as compared to the involvement of lattice oxygen. Moreover, the simulations confirm the presence of Co^{3+} centers both at the fivefold coordinated octahedral surface sites as well as underneath adsorbed ROS and 2-propoxide. An interesting feature is that the surface Co^{3+} switch from intermediate to low spin upon adsorption of ROS and 2-propoxide. Sojka and co-workers[56] described the reactivity of surface ROS in the oxidation of CH_4 and CO over Co_3O_4 (100) and associate surface ROS varieties like molecular oxygen ad-species and monoatomic oxygen species with the ability to oxidize CO and activate C-H bonds, respectively. Later the same

group studied the interplay of the Langmuir-Hinshelwood and the Mars-van Krevelen mechanisms for CH_4 oxidation depending on the redox state of Co_3O_4 and the involvement of adsorbed or lattice oxygen.[57] Thus, the Co_3O_4 surface state diagram is a useful thermodynamic reference for the distinction of Langmuir-Hinshelwood and Mars-van Krevelen mechanisms for catalytic oxidation processes on cobalt spinels.

Scheme 1. Reaction pathway of selective 2-propanol oxidation involving nucleophilic atomic oxygen species**.**

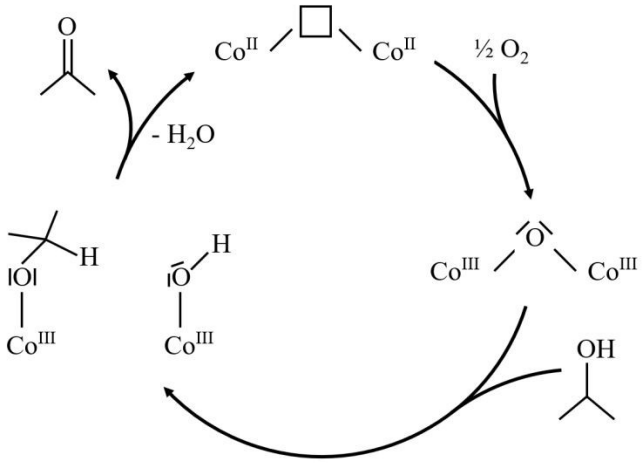

5. CONCLUSION

Phase-pure crystalline spinel cobalt oxide Co_3O_4 nanoparticles were successfully synthesized by the decomposition of cobalt acetylacetonate in oleyl amine followed by calcination. The resulting bulk Co_3O_4 was found to be a highly active and selective catalyst for 2-propanol oxidation. The unsupported Co_3O_4 nanoparticles catalyze the oxidative dehydrogenation of 2-propanol to acetone as main product even below 373 K. Up to 573 K the selectivity only drops slightly due to the formation of the total oxidation product CO_2. Co_3O_4 nanoparticles showed remarkable results reaching almost full conversion with 100% selectivity to acetone already at 430 K during the first oxidation run. The low-temperature activity can be restored by an oxidative treatment and is attributed to the $Co^{2+/3+}$ redox couple

in close connection to reactive surface oxygen species, identified by XAS, XPS and TPO, O_2 TPD, and theoretical calculations.

ASSOCIATED CONTENT

Supporting Information

The Supporting information is available free of charge on the ACS Publication website at http://pubs.acs.org.

Adsorption-/desorption isotherms, TPO profile after 2-propanol oxidation, deconvoluted O 1s spectra before and after 2-propanol oxidation, Co K-edge XANES spectra under 2-propanol decomposition conditions, Co K-edge EXAFS spectra of before and after 2-propanol decomposition, and best fit EXAFS parameters.

AUTHOR INFORMATION

Corresponding Author

*E-mail: muhler@techem.rub.de

Author Contributions

The manuscript was written through contributions of all authors. All authors have given approval to the final version of the manuscript.

Funding Sources

This research was funded by the Deutsche Forschungsgemeinschaft (DFG, German Research Foundation) – Projektnummer 388390466 – TRR 247 within the collaborative research center/transregio 247 "Heterogeneous Oxidation Catalysis in the Liquid Phase". Funding from

the European Research Council under grant ERC-OPERANDOCAT (ERC-725915) is also acknowledged.

Notes

The authors declare no competing financial interest.

ACKNOWLEDGMENTS

The DFG core facility ICAN are gratefully acknowledged for performing the TEM characterization. Authors thank Lukas Pielsticker (RUB) as well as beamline staff at ALBA synchrotron, in particular, Dr. Carlo Marini and Dr. Nitya Ramanan, for their help during XAFS measurements. We acknowledge computational time at the MagnitUDE supercomputer (DFG grants INST 20876/209-1 FUGG, INST20876/243-1 FUGG).

REFERENCES

(1) Kamal, M. S.; Razzak, S. A.; Hossain, M. M. Catalytic oxidation of volatile organic compounds (VOCs) – A review. *Atmos. Environ.* **2016**, *140*, 117–134.

(2) Zhang, Z.; Jiang, Z.; Shangguan, W. Low-temperature catalysis for VOCs removal in technology and application. *Catal. Today* **2016**, *264*, 270–278.

(3) Huang, H.; Xu, Y.; Feng, Q.; Leung, D. Y. C. Low temperature catalytic oxidation of volatile organic compounds. *Catal. Sci. Technol.* **2015**, *5*, 2649–2669.

(4) Bürgi, T.; Bieri, M. Time-Resolved in Situ ATR Spectroscopy of 2-Propanol Oxidation over Pd/Al_2O_3. *J. Phys. Chem. B* **2004**, *108*, 13364–13369.

(5) Centeno, M.A.; Paulis, M.; Montes, M.; Odriozola, J.A. Catalytic combustion of volatile organic compounds on $Au/CeO_2/Al_2O_3$ and Au/Al_2O_3 catalysts. *Appl. Catal., A* **2002**, *234*, 65–78.

(6) Liu, S. Y.; Yang, S. M. Complete oxidation of 2-propanol over gold-based catalysts supported on metal oxides. *Appl. Catal., A* **2008**, *334*, 92–99.

(7) Minicò, S.; Scirè, S.; Crisafulli, C.; Galvagno, S. Influence of catalyst pretreatments on volatile organic compounds oxidation over gold/iron oxide. *Appl. Catal., B* **2001**, *34*, 277–285.

(8) Biella, S.; Rossi, M. Gas phase oxidation of alcohols to aldehydes or ketones catalysed by supported gold. *Chem. Commun.* **2003**, *3*, 378–379.

(9) Gong, J.; Flaherty, D. W.; Yan, T.; Mullins, C. B. Selective oxidation of propanol on Au(111): mechanistic insights into aerobic oxidation of alcohols. *ChemPhysChem* **2008**, *9*, 2461–2466.

(10) Wiegand, B. C.; Uvdal, P.; Serafin, J. G.; Friend, C. M. Isotopic Labeling as a Tool to Establish Intramolecular Vibrational Coupling: The Reaction of 2-Propanol on Mo(110). *J. Phys. Chem. A* **1992**, *96*, 5063–5069.

(11) Tian, Z.-Y.; Mountapmbeme Kouotou, P.; El Kasmi, A.; Tchoua Ngamou, P. H.; Kohse-Höinghaus, K.; Vieker, H.; Beyer, A.; Gölzhäuser, A. Low-temperature deep oxidation of olefins and DME over cobalt ferrite. *P. Combust. Inst.* **2015**, *35*, 2207–2214.

(12) Urdă, A.; Herraïz, A.; Rédey, Á.; Marcu, I.-C. Co and Ni ferrospinels as catalysts for propane total oxidation. *Catal. Commun.* **2009**, *10*, 1651–1655.

(13) Mountapmbeme Kouotou, P.; Vieker, H.; Tian, Z. Y.; Tchoua Ngamou, P. H.; El Kasmi, A.; Beyer, A.; Gölzhäuser, A.; Kohse-Höinghaus, K. Structure–activity relation of spinel-type Co–Fe oxides for low-temperature CO oxidation. *Catal. Sci. Technol.* **2014**, *4*, 3359.

(14) Thomas, J.; Thomas, N.; Girgsdies, F.; Beherns, M.; Huang, X.; Sudheesh, V. D.; Sebastian, V. Synthesis of cobalt ferrite nanoparticles by constant pH co-precipitation and their high catalytic activity in CO oxidation. *New J. Chem.* **2017**, *41*, 7356–7363.

(15) Xie, X.; Li, Y.; Liu, Z.-Q.; Haruta, M.; Shen, W. Low-temperature oxidation of CO catalysed by Co_3O_4 nanorods. *Nature* **2009**, *458*, 746–749.

(16) Omata, K.; Takada, T.; Kasahara, S.; Yamada, M. Active site of substituted cobalt spinel oxide for selective oxidation of COH_2. Part II. *Appl. Catal., A* **1996**, *146*, 255–267.

(17) Evans, G.; Kozhevnikov, I. V.; Kozhevnikova, E. F.; Claridge, J. B.; Vaidhyanathan, R.; Dickinson, C.; Wood, C. D.; Cooper, A. I.; Rosseinsky, M. J. Particle size–activity relationship for $CoFe_2O_4$ nanoparticle CO oxidation catalysts. *J. Mater. Chem.* **2008**, *18*, 5518.

(18) Chagas, C. A.; Souza, E. F. de; Carvalho, M. C.N.A. de; Martins, R. L.; Schmal, M. Cobalt ferrite nanoparticles for the preferential oxidation of CO. *Appl. Catal., A* **2016**, *519*, 139–145.

(19) Lukashuk, L.; Föttinger, K.; Kolar, E.; Rameshan, C.; Teschner, D.; Hävecker, M.; Knop-Gericke, A.; Yigit, N.; Li, H.; McDermott, E.; Stöger-Pollach, M.; Rupprechter, G. Operando XAS and NAP-XPS studies of preferential CO oxidation on Co_3O_4 and CeO_2-Co_3O_4 catalysts. *J. Catal.* **2016**, *344*, 1–15.

(20) Bahlawane, N.; Ngamou, P. H. T.; Vannier, V.; Kottke, T.; Heberle, J.; Kohse-Hoinghaus, K. Tailoring the properties and the reactivity of the spinel cobalt oxide. *Phys. Chem. Chem. Phys.* **2009**, *11*, 9224–9232.

(21) Tian, Z.-Y.; Tchoua Ngamou, P. H.; Vannier, V.; Kohse-Höinghaus, K.; Bahlawane, N. Catalytic oxidation of VOCs over mixed Co–Mn oxides. *Appl. Catal., B* **2012**, *117-118*, 125–134.

(22) Hosseini, S. A.; Salari, D.; Niaei, A.; Deganello, F.; Pantaleo, G.; Hojati, P. Chemical-physical properties of spinel $CoMn_2O_4$ nano-powders and catalytic activity in the 2-propanol and toluene combustion: Effect of the preparation method. *J. Environ. Sci. Health., Part A* **2011**, *46*, 291–297.

(23) Ortega, K. F.; Anke, S.; Salamon, S.; Özcan, F.; Heese, J.; Andronescu, C.; Landers, J.; Wende, H.; Schuhmann, W.; Muhler, M.; Lunkenbein, T.; Behrens, M. Topotactic Synthesis of Porous Cobalt Ferrite Platelets from a Layered Double Hydroxide Precursor and Their Application in Oxidation Catalysis. *Chem. Eur. J.* **2017**, *263*, 80.

(24) Zafeiratos, S.; Dintzer, T.; Teschner, D.; Blume, R.; Hävecker, M.; Knop-Gericke, A.; Schlögl, R. Methanol oxidation over model cobalt catalysts. *J. Catal.* **2010**, *269*, 309–317.

(25) Gu, D.; Jia, C.-J.; Weidenthaler, C.; Bongard, H.-J.; Spliethoff, B.; Schmidt, W.; Schüth, F. Highly Ordered Mesoporous Cobalt-Containing Oxides. *J. Am. Chem. Soc.* **2015**, *137*, 11407–11418.

(26) Finocchio, E.; Willey, R. J.; Busca, G.; Lorenzelli, V. FTIR studies on the selective oxidation and combustion of light hydrocarbons at metal oxide surfaces. *J. Chem. Soc., Faraday Trans.* **1997**, *93*, 175–180.

(27) Finocchio, E.; Busca, G.; Lorenzelli, V.; Escribano, V. S. FTIR studies on the selective oxidation and combustion of light hydrocarbons at metal oxide surfaces. *J. Chem. Soc., Faraday Trans.* **1996**, *92*, 1587–1593.

(28) Busca, G.; Guidetti, R.; Lorenzelli, V. Fourier-transform Infrared Study of the Surface Properties of Cobalt Oxides. *J. Chem. Soc., Faraday Trans.* **1990**, *86*, 989–994.

(29) Busca, G.; Daturi, M.; Finocchio, E.; Lorenzelli, V.; Ramis, G.; Willey, R. J. Transition metal mixed oxides as combustion catalysts: preparation, characterization and activity mechanisms. *Catal. Today* **1997**, *33*, 239–249.

(30) Solsona, B.; García, T.; Hutchings, G. J.; Taylor, S. H.; Makkee, M. TAP reactor study of the deep oxidation of propane using cobalt oxide and gold-containing cobalt oxide catalysts. *Appl. Catal., A* **2009**, *365*, 222–230.

(31) Zasada, F.; Piskorz, W.; Janas, J.; Budiyanto, E.; Sojka, Z. Dioxygen Activation Pathways over Cobalt Spinel Nanocubes - From Molecular Mechanism into Ab Initio Thermodynamics and $^{16}O_2/^{18}O_2$ Exchange Microkinetics. *J. Phys. Chem. C* **2017**, *121*, 24128–24143.

(32) Shojaee, K.; Montoya, A.; Haynes, B. S. Insight into oxygen stability and vacancy formation on Co_3O_4 model slabs. *Comput. Mater. Sci.* **2013**, *72*, 15–25.

(33) Takita, Y.; Tashiro, T.; Saito, Y.; Hori, F. The Effects of Water Coadsorption on the adsorption of Oxygen over Metal Oxides. *J. Catal.* **1986**, *97*, 25–35.

(34) Asano, K.; Ohnishi, C.; Iwamoto, S.; Shioya, Y.; Inoue, M. Potassium-doped Co_3O_4 catalyst for direct decomposition of N_2O. *Appl. Catal. B* **2008**, *78*, 242–249.

(35) Iwamoto, M.; Yoda, Y.; Yamazoe, N.; Seiyama, T. Study of metal oxide catalysts by temperature programmed desorption. 4. Oxygen adsorption on various metal oxides. *J. Phys. Chem.* **1978**, *82*, 2564–2570.

(36) Simonelli, L.; Marini, C.; Olszewski, W.; vila Prez, M.; Ramanan, N.; Guilera, G.; Cuartero, V.; Klementiev, K.; Saini, N. L. CLÆSS: The hard X-ray absorption beamline of the ALBA CELLS synchrotron. *Cogent Physics* **2016**, *3*, 1510.

(37) Ravel, B.; Newville, M. ATHENA, ARTEMIS, HEPHAESTUS: data analysis for X-ray absorption spectroscopy using IFEFFIT. *J. Synchrotron Radiat.* **2005**, *12*, 537–541.

(38) Kresse, G.; Hafner, J. Ab initio molecular-dynamics simulation of the liquid-metal-amorphous-semiconductor transition in germanium. *Phys. Rev. B: Condens. Matter Mater. Phys.* **1994**, *49*, 14251–14269.

(39) Kresse, G.; Furthmüller, J. Efficiency of ab-initio total energy calculations for metals and semiconductors using a plane-wave basis set. *Comput. Mater. Sci.* **1996**, *6*, 15–50.

(40) Kresse, G.; Furthmüller, J. Efficient iterative schemes for ab initio total-energy calculations using a plane-wave basis set. *Phys. Rev. B: Condens. Matter Mater. Phys.* **1996**, *54*, 11169–11186.

(41) Blöchl, P. E. Projector augmented-wave method. *Phys. Rev. B: Condens. Matter Mater. Phys.* **1994**, *50*, 17953–17979.

(42) Perdew, J. P.; Wang, Y. Accurate and simple analytic representation of the electron-gas correlation energy. *Phys. Rev. B* **1992**, *45*, 13244–13249.

(43) Dudarev, S. L.; Botton, G. A.; Savrasov, S.; Humphreys, C. J.; Sutton, A. P. Electron-energy-loss spectra and the structural stability of nickel oxide: An LSDA+U study. *Phys. Rev. B: Condens. Matter Mater. Phys.* **1998**, *57*, 1505–1509.

(44) Hajiyani, H.; Pentcheva, R. Surface Termination and Composition Control of Activity of the $Co_xNi_{1-x}Fe_2O_4$ (001) Surface for Water Oxidation. *ACS Catal.* **2018**, *8*, 11773–11782.

(45) Rouquerol, R.; Rouquerol, J.; Sing, K. *Adsorption by Powders &; Porous Solids;* Academic Press: London, 1999.

(46) Broqvist, P. A DFT Study on CO Oxidation over Co_3O_4. *J. Catal.* **2002**, *210*, 198–206.

(47) Piskorz, W.; Zasada, F.; Stelmachowski, P.; Kotarba, A.; Sojka, Z. Decomposition of N_2O over the surface of cobalt spinel. *Catal. Today* **2008**, *137*, 418–422.

(48) Zasada, F.; Piskorz, W.; Sojka, Z. Cobalt Spinel at Various Redox Conditions. *J. Phys. Chem. C* **2015**, *119*, 19180–19191.

(49) Novotny, Z.; Mulakaluri, N.; Edes, Z.; Schmid, M.; Pentcheva, R.; Diebold, U.; Parkinson, G. S. Probing the surface phase diagram of Fe_3O_4 (001) towards the Fe-rich limit. *Phys. Rev. B* **2013**, *87*, 195410–195418.

(50) Biesinger, M. C.; Payne, B. P.; Grosvenor, A. P.; Lau, L. W.M.; Gerson, A. R.; Smart, R. S.C. Resolving surface chemical states in XPS analysis of first row transition metals, oxides and hydroxides. *Appl. Surf. Sci.* **2011**, *257*, 2717–2730.

(51) Yang, J.; Liu, H.; Martens, W. N.; Frost, R. L. Synthesis and Characterization of Cobalt Hydroxide, Cobalt Oxyhydroxide, and Cobalt Oxide Nanodiscs. *J. Phys. Chem. C* **2010**, *114*, 111–119.

(52) Mathew, T. Cu–Co Synergism in $Cu_{1-x}Co_xFe_2O_4$ - Catalysis and XPS Aspects. *J. Catal.* **2002**, *210*, 405–417.

(53) Anantharamaiah, P. N.; Joy, P. A. Enhancing the strain sensitivity of $CoFe_2O_4$ at low magnetic fields without affecting the magnetostriction coefficient by substitution of small amounts of Mg for Fe. *Phys. Chem. Chem. Phys.* **2016**, *18*, 10516–10527.

(54) Roth, W. L. The magnetic structure of Co_3O_4. *J. Phys. Chem. Solids* **1964**, *25*, 1–10.

(55) Calvin, S.; Miller, M. M.; Goswami, R.; Cheng, S.-F.; Mulvaney, S. P.; Whitman, L. J.; Harris, V. G. Determination of crystallite size in a magnetic nanocomposite using extended x-ray absorption fine structure. *J. Appl. Phys.* **2003**, *94*, 778–783.

(56) Zasada, F.; Piskorz, W.; Janas, J.; Gryboś, J.; Indyka, P.; Sojka, Z. Reactive Oxygen Species on the (100) Facet of Cobalt Spinel Nanocatalyst and their Relevance in $^{16}O_2/^{18}O_2$ Isotopic Exchange, *de*N_2O, and *de*CH_4 Processes - A Theoretical and Experimental Account. *ACS Catal.* **2015**, *5*, 6879–6892.

(57) Zasada, F.; Janas, J.; Piskorz, W.; Gorczyńska, M.; Sojka, Z. Total Oxidation of Lean Methane over Cobalt Spinel Nanocubes Controlled by the Self-Adjusted Redox State of the Catalyst. *ACS Catal.* **2017**, *7*, 2853–2867.

DOI: 10.1021/acscatal.9b01048
URN: urn:nbn:de:hbz:464-20210127-144420-9

This document is the Accepted Manuscript version of a Published Work that appeared in final form in: *ACS Catal.* 2019, 9, 7, 5974–5985, copyright © American Chemical Society after peer review and technical editing by the publisher.
To access the final edited and published work see: https://doi.org/10.1021/acscatal.9b01048